Multiband effective bond-orbital model for nitride semiconductors with wurtzite structure

Daniel Mourad,* Stefan Barthel, and Gerd Czycholl
Institute for Theoretical Physics, University of Bremen, D-28359 Bremen, Germany

(Received 12 January 2010; revised manuscript received 19 March 2010; published 22 April 2010)

A multiband empirical tight-binding model for group-III-nitride semiconductors with a wurtzite structure has been developed and applied to both bulk systems and embedded quantum dots. As a minimal basis set, we assume one *s* orbital and three *p* orbitals, localized in the unit cell of the hexagonal Bravais lattice, from which one conduction band and three valence bands are formed. Nonvanishing matrix elements up to second-nearest neighbors are taken into account. These matrix elements are determined so that the resulting tight-binding band structure reproduces the known Γ-point parameters, which are also used in recent $\mathbf{k}\cdot\mathbf{p}$ treatments. Furthermore, the tight-binding band structure can also be fitted to the band energies at other special symmetry points of the Brillouin-zone boundary, known from experiment or from first-principles calculations. In this paper, we describe details of the parametrization and present the resulting tight-binding band structures of bulk GaN, AlN, and InN with a wurtzite structure. As a first application to nanostructures, we present results for the single-particle electronic properties of lens-shaped InN quantum dots embedded in a GaN matrix.

DOI: 10.1103/PhysRevB.81.165316 PACS number(s): 78.67.Hc, 73.22.Dj, 71.15.Ap, 73.21.La

I. INTRODUCTION

Due to their unique physical properties, zero-dimensional semiconductor nanostructures, realized by either epitaxial growth or colloidal chemical synthesis,[1] offer a broad range of applications.[2] The three-dimensional confinement of spatially localized charge carriers in such tailor-made systems leads to a discrete and tunable one-particle spectrum, which can be used for a variety of optoelectronic applications, for quantum computing and quantum cryptography, and even for nanobiological applications such as biological fluorescence labeling.[3,4]

Most binary group II-VI and III-V semiconductor materials and their ternary and quaternary alloys crystallize in the cubic zinc blende or in the hexagonal wurtzite phase so the corresponding nanostructures can also be attributed to one of these two structures. Dependent on the material system and the adequate parameter range of the experimental conditions (e.g., growth temperature and substrate type for epitaxial growth, additionally the chemical environment and particle size for colloidal synthesis), it is even possible nowadays to realize either of the two structures for the same compounds. For example, epitaxially grown GaN/AlN quantum dots can be produced in the metastable zinc blende modification and in the thermodynamically stable wurtzite configuration.[5]

The calculation of the optical properties of such systems requires the knowledge of a set of single-particle eigenstates and eigenvalues for the confined carriers (electrons and holes), which can be obtained by means of different methods. Rather simple models such as effective mass approximations[6–8] can give a distinct insight into the behavior of such systems. Multiband $\mathbf{k}\cdot\mathbf{p}$ models[9–12] incorporate higher effects such as valence-band mixing but still make use of the envelope function approximation, thus not resolving the characteristic underlying lattice structure. Nevertheless, they have been successfully applied to various material systems and were extended by the inclusion of strain and piezoelectricity effects.

Empirical pseudopotential models (EPMs) (Refs. 13–16) and empirical tight-binding models (ETBMs)[17–22] allow for the possibility of a microscopic description of nanostructures. While the EPM is capable of resolving variations on the atomic scale, it requires a large set of basis states, which limits the application of these models to small nanostructures. The ETBM uses a coarse graining on the scale of lattice sites, which makes it possible to stick to a small set of basis states and perform calculations on larger supercells with feasible effort. Additionally, it gives a rather intuitive real-space picture of the system in terms of localized Wannier states. The coupling between different lattice sites is usually limited to first- or second-nearest neighbors, depending on the purpose. The goal is to analytically deduce a manageable set of equations for the TB matrix elements in terms of bulk parameters (e.g., the band gap, effective masses, and spin-orbit splitting) which can be accessed either from experiment or from first-principles calculations such as DFT-LDA or recent G_0W_0 results.[23,24] These TB matrix elements then enter the nanostructure calculation.

When establishing an empirical tight-binding model, one can start from a Löwdin-orthogonalized atomic basis and use a linear combination of atomic orbitals (LCAO) as ansatz for the required eigenstates.[25] For nitride semiconductors with a wurtzite structure, this has been done recently by Schulz *et al.*[19] But it is as well justified to start from "effective bond orbitals," i.e., Wannier-type orbitals localized within a unit cell. Within the LCAO spirit, these effective orbitals can, in principle, be expressed as linear combinations of the above-mentioned atomic orbitals. Neither the atomic orbitals nor the effective orbitals are explicitly known or required within an empirical TB approach, as only the matrix elements between those orbitals are needed to obtain the TB band structure. Therefore, it is equally justified to perform the parametrization directly for the effective bond orbitals so that known bulk band-structure properties are reproduced. Such a version of an ETBM is commonly called "effective bond-orbital model" (EBOM). The EBOM has the advantage that it usually allows for a better fit throughout the whole Brillouin zone (BZ) within a given basis set.

The EBOM has long been established for the cubic zinc-blende structure; a first EBOM parametrization by Chang[26]

 ©2010 The American Physical Society

incorporated three-center overlap integrals in a basis set of one s and three p orbitals on each site of the fcc Bravais lattice. This parametrization was restricted to coupling up to nearest neighbors so that only the band energies at the Γ point were fitted, besides the usual set of effective conduction band masses and corresponding valence-band parameters. Loehr augmented this model in Ref. 27 by the inclusion of hopping up to second-nearest neighbors to additionally fit the band structure of the bulk material to an extended parameter set, including the X-point energies. This resulted in a better agreement of the resulting tight-binding conduction band with first-principles calculations.[28]

To our knowledge, there exists only one parametrization of the EBOM for materials with wurtzite structure in the literature.[29] As this work is restricted to a nearest-neighbor parametrization and a fit to zone-center energies only, we developed a new parametrization including second-nearest-neighbor matrix elements and a fit to band energies at other special BZ points. We apply this EBOM to the calculation of the electronic properties of lens-shaped InN quantum dots embedded within GaN.

This work is organized as follows. In Sec. II, our specific EBOM is presented. We developed a second-nearest-neighbor parametrization. Furthermore, we describe the application to zero-dimensional nanostructures and discuss the inclusion of strain and piezoelectric fields. In Sec. III, the one-particle spectrum for a lens-shaped InN quantum dot embedded within GaN and a comparison with results from other $\mathbf{k}\cdot\mathbf{p}$ and fully microscopic ETBM calculations is given. Section IV contains a summary, a conclusion and a brief outlook to possible extensions of our model.

II. THEORY

A. Effective bond-orbital model for bulk semiconductors

Linear combinations of atomic orbitals within one unit cell can be used as ansatz for the Wannier functions localized within the unit cell of the Bravais lattice. From these Wannier functions, the extended Bloch functions can be determined by means of a unitary transformation. As neither the atomic states nor the Wannier functions are explicitly used in an empirical tight-binding model, it is not necessary to start from the atomic wave functions but one can directly assume a basis of Wannier-type functions, which is the basic idea of the EBOM approach.

As the conduction-band wave functions at the BZ center predominantly transform s-like with some p_z character while the corresponding valence-band wave functions transform like p states with some s character, we use a localized sp^3 basis per spin direction,

$$|\mathbf{R},\alpha\rangle, \alpha \in \{s\uparrow, p_x\uparrow, p_y\uparrow, p_z\uparrow, s\downarrow, p_x\downarrow, p_y\downarrow, p_z\downarrow\}. \quad (1)$$

Here $\mathbf{R}$ labels the N sites of the hexagonal lattice, which is the underlying Bravais lattice of the wurtzite crystal structure.

A trial wave function that satisfies the Bloch condition is the Bloch sum,

$$|\psi_{\mathbf{k}}\rangle = \frac{1}{\sqrt{N}}\sum_{\alpha} c_{\alpha}(\mathbf{k})\sum_{\mathbf{R}} e^{i\mathbf{k}\cdot\mathbf{R}}|\mathbf{R},\alpha\rangle. \quad (2)$$

The band structure $E(\mathbf{k})$ is now given by the solution of the secular equation,

$$\sum_{\alpha'} H_{\alpha\alpha'}(\mathbf{k})c_{\alpha'}(\mathbf{k}) = E(\mathbf{k})c_{\alpha}(\mathbf{k}), \quad (3)$$

for each wave vector $\mathbf{k}$, where

$$H_{\alpha\alpha'}(\mathbf{k}) = \sum_{\mathbf{R},\mathbf{R}'} e^{i\mathbf{k}\cdot(\mathbf{R}-\mathbf{R}')}E_{\alpha\alpha'}^{\mathbf{R}\mathbf{R}'}. \quad (4)$$

The EBOM matrix elements of the bulk Hamiltonian H^{bulk} are thus given by

$$E_{\alpha\alpha'}^{\mathbf{R}\mathbf{R}'} = \langle\mathbf{R},\alpha|H^{\text{bulk}}|\mathbf{R}',\alpha'\rangle. \quad (5)$$

It should explicitly be pointed out that the artificial change in point-group symmetry from C_{3v} (wurtzite) to C_{6v} (hexagonal lattice) in the EBOM approach does *not* uniquely stem from the omission of the atomic basis but rather from the specific set of basis functions used. For instance, the original inversion asymmetry of the wurtzite crystal could be restored when the set of basis functions, Eq. (1), is extended by states that are not parity eigenstates. This has been done for cubic systems by Cartoixà *et al.* in Ref. 30.

To include the influence of spin-orbit coupling, we follow Ref. 31. As we expect the spin-orbit part of H_{bulk} to be of weak influence, we assume only site-diagonal contributions, which stem from the p orbitals. Additionally, the nonideal c/a lattice constant ratio energetically separates the p_z- from the p_x- and the p_y orbitals. These effects can properly be incorporated by introduction of one spin-orbit splitting parameter Δ_{so} and one crystal field splitting parameter Δ_{cr}.

When restricting the nonvanishing matrix elements, Eq. (5), up to nearest or second-nearest neighbors, the secular equation (3) can be solved analytically for high-symmetry points throughout the BZ of the hexagonal lattice. This yields a set of equations for the EBOM matrix elements in terms of the energetic positions of the bands at the critical $\mathbf{k}$ values. By expanding the elements of Eq. (4) around the BZ center and comparing the matrix representation to a corresponding $\mathbf{k}\cdot\mathbf{p}$ Hamiltonian,[32,33] it is possible to deduce additional constraints in terms of the conduction-band effective masses and corresponding valence-band parameters.

The goal is to arrive at a solvable set of equations which link a sufficiently large number of $E_{\alpha\alpha'}^{\mathbf{R}\mathbf{R}'}$ to a desired set of band-structure parameters. In practice, this will require the additional omission of either matrix elements or band parameters, as the system of equations becomes rather complicated. The low symmetry of the hexagonal lattice will result in a larger number of independent parameters and equations than in the case of cubic crystal systems. An overview of the results for a coupling up to second-nearest neighbors is given in Table I. More details on the parametrization are given in Appendix.

TABLE I. Overview of the EBOM parametrization with coupling up to second-nearest neighbors. The nomenclature for the band energies follows the usual single group notation, see, e.g., Ref. 34. Note that an additional valence-band parameter A_7 has been neglected.

Second-nearest-neighbor coupling: 26 EBOM matrix elements	
Band parameter	Description
$E_g=\Gamma_1^c-\Gamma_6^v$	Direct band gap at Γ
$m_e^{\parallel}$, $m_e^{\perp}$	Effective electron masses
A_1, A_2, A_3, A_4, A_5, A_6	Valence band parameters
Δ_{so}	Spin-orbit splitting
Δ_{cr}	Crystal field splitting
$A_{1,3}^c$, $A_{5,6}^v$, $A_{1,3}^v$	A-point energies
$L_{1,3}^c$, $L_{1,3}^v$, $L_{2,4}^v$, $L_{1,3'}^v$	L-point energies
M_1^c, M_4^v, M_3^v, M_1^v	M-point energies
H_3^c, H_3^v, $H_{3'}^v$	H-point energies
$E_p^{\parallel,\perp}=f(E_g,\Delta_{so},\Delta_{cr},m^{\parallel,\perp})$	Kane parameters

The band structure for this parametrization is now obtained by the diagonalization of the 8×8 matrix $H_{\alpha\alpha'}(\mathbf{k})$, Eq. (4), for each $\mathbf{k}$.

For all calculations in the present paper, two distinct parameter sets have been used. The first parameter set is derived from a consistent set of band parameters[24] obtained from G_0W_0 calculations based on exact-exchange optimized effective potential (OEPx) ground states,[35] supplemented by additional band-structure energies at high-symmetry points.[36] Since the G_0W_0@OEPx band gaps and crystal field splittings still differ slightly from the experimental values, we decided to use a second parameter set in which these values were replaced by the parameters recommended by Vurgaftman and Meyer in 2003.[37] To obtain the correct band gaps, all conduction-band energies from the G_0W_0 calculations were shifted by the respective difference in the second parameter set. Moreover, we used the spin-orbit splittings of Ref. 37 in both sets, as the G_0W_0 calculations did not include the electron spin. This should be a reasonable approach, as the spin-orbit splitting is comparatively small in these systems. The two parameter sets are listed in Table II and will be referred to simply as "G_0W_0 parameters" and "corrected G_0W_0 parameters" from now on.

In our opinion, the corrected G_0W_0 parameters should clearly be preferred, as it is known that even highly sophisticated *ab initio* approaches still do not properly reproduce the band gap.

The resulting band structures are depicted in Fig. 1 for AlN, InN, and GaN. The top of the valence band of each material is set to zero. One can easily identify the direct band gap in the Brillouin-zone center, one spin-degenerate conduction band and three spin-degenerate valence bands, according to the employed basis set, Eq. (1), of four orbitals per spin direction. The twofold Kramers degeneracy of each energy level $E(\mathbf{k})$ is a direct consequence of the time-reversal symmetry, as no external magnetic field is applied. Due to the fitting to the multiple high-symmetry points on the BZ surface, each band has a finite bandwidth of a realistic magnitude, which the $\mathbf{k}\cdot\mathbf{p}$ theory, of course, does not reproduce, as it is restricted to the vicinity of the BZ center within this basis set. In addition, no erroneous curvature of the bands into the band gap occurs for larger $|\mathbf{k}|$.

At first glance, the band structures do not differ significantly for both parameter sets. To emphasize the differences, Fig. 2 shows the band structure of InN around the Γ point. By having a closer look, one can see that the energetic positions are different, because of the different crystal field splitting and band gap. Also, the curvatures of the bands differ for the two parameter sets. This is a result of the slightly different $E_p^{\parallel,\perp}$ and will be addressed again in Sec. III B. More sophisticated methods for band-structure calculation will give more conduction and valence bands in the energetic range around the band gap. Although this feature could also be included in our EBOM approach by augmenting the number of orbitals per unit cell, it would not only result in a more complicated parametrization but also lead to significantly higher computational costs for nanostructure calculations. Thus we stick to a minimal basis set of four bands per spin direction, which gives a reasonable agreement with the "true" band structure in the region of interest. The reliability of this basis set has also been established by the variety of existing eight-band $\mathbf{k}\cdot\mathbf{p}$ calculations for these systems and comparisons to experimental results for device applications.[32,38]

Of course, our EBOM parametrization is not limited to a specific set of parameters. The fit to the energies at the BZ boundaries allows for an adaption to a wide range of parameters, as these additional constraints practically prevent spurious solutions where the bands curve into the band gap far away from the BZ center. These problems are widely known to occur for simpler $\mathbf{k}\cdot\mathbf{p}$ and tight-binding parametrizations when an inappropriate set of Γ-point parameters is used.

With our model, a more systematic investigation of the influence of single parameters on the properties of low-dimensional systems is possible, as the band structure is not sensitive to small perturbations in the input parameters. This stability of the parametrization transfers directly to the application on nanostructures, as, e.g., spurious solutions in the bulk band gap will lead to corresponding states in the forbidden energy region of the nanostructure. In spite of the progress in the field of both sophisticated *ab initio* calculations and highly refined experiments, this is and will remain an important feature, as certain physical quantities such as band offsets, Luttinger parameters, and optical matrix elements remain ambiguous because they are only indirectly measurable and depend on model assumptions.

B. Application of the EBOM to quantum dots

As we now have determined the EBOM matrix elements for the bulk materials, they can be used as input in the calculations for a quantum-confined nanostructure. In case of a quantum dot, the translational invariance is lost in all three spatial dimensions so the adequate ansatz for an eigenstate, Eq. (2), is reduced to a direct linear combination of localized

TABLE II. Empirical parameter sets used in the EBOM calculations. The first parameter set corresponds to results obtained in a DFT+G_0W_0 treatment by Rinke *et al.* (Refs. 24 and 36) while the second parameter set replaces some parameters by values recommended by Vurgaftman *et al.* (Ref. 37). See the text for further discussion. Blank cells mean the adoption of the parameter of the alternate set.

Reference	G_0W_0 parameters			Corrected G_0W_0 parameters		
Material	AlN	GaN	InN	AlN	GaN	InN
a (Å)	3.110	3.190	3.540			
c (Å)	4.980	5.189	5.706			
E_g (eV)	6.464	3.239	0.694	6.250	3.510	0.78
Δ_{so} (eV)				0.019	0.017	0.005
Δ_{cr} (eV)	−0.295	0.034	0.066	−0.169	0.010	0.040
$E_p^{\parallel}$ (eV)	16.972[a]	17.292[a]	8.742[a]		$f(E_g,\Delta_{so},\Delta_{cr},m^{\parallel})$	
$E_p^{\perp}$ (eV)	18.165[a]	16.265[a]	8.809[a]		$f(E_g,\Delta_{so},\Delta_{cr},m^{\perp})$	
$m_e^{\parallel}$ (m_0)	0.322[a]	0.186[a]	0.065[a]			
$m_e^{\perp}$ (m_0)	0.329[a]	0.209[a]	0.068[a]			
A_1	−3.991	−5.947	−15.803			
A_2	−0.311	−0.528	−0.497			
A_3	3.671	5.414	15.251			
A_4	−1.147	−2.512	−7.151			
A_5	−1.329	−2.510	−7.060			
A_6	−1.952	−3.202	−10.078			
$A_{1,3}^c$ (eV)	8.844	5.701	3.355	8.631	5.972	3.441
$A_{5,6}^v$ (eV)	−0.686	−0.597	−0.509			
$A_{1,3}^v$ (eV)	−3.573	−4.110	−3.581			
$L_{1,3}^c$ (eV)	7.545	5.798	4.356	7.332	6.069	4.442
$L_{1,3}^v$ (eV)	−1.515	−2.065	−1.732			
$L_{2,4}^v$ (eV)	−1.689	−2.144	−1.838			
$L_{1,3'}^v$ (eV)	−6.033	−6.984	−5.769			
M_1^c (eV)	8.084	6.550	4.934	7.870	6.821	5.020
M_4^v (eV)	−0.837	−1.111	−0.997			
M_3^v (eV)	−1.893	−2.382	−1.889			
M_1^v (eV)	−3.649	−4.518	−3.714			
H_3^c (eV)	9.774	7.982	6.281	9.560	8.253	6.367
H_3^v (eV)	−0.914	−1.609	−1.401			
$H_{3'}^v$ (eV)	−5.202	−6.474	−5.422			

[a]For a given band gap, $E_p^{\parallel,\perp}$ are not independent parameters when $m^{\parallel,\perp}$ are known [see Eqs. (A1)–(A3)] in Appendix. To obtain a better fit to the G_0W_0 band structure, these parameters can be adjusted by least-squares fit values, see Ref. 24. When the band gap is subsequently altered, as in the set to the right, the analytic expression has to be used again.

effective orbitals,

$$|\psi\rangle = \sum_{\alpha,\mathbf{R}} c_{\mathbf{R}\alpha}|\mathbf{R},\alpha\rangle. \qquad (6)$$

The corresponding secular equation is now given by

$$\sum_{\alpha',\mathbf{R}'} E_{\alpha\alpha'}^{\mathbf{RR}'} c_{\mathbf{R}'\alpha'} = E c_{\mathbf{R}\alpha}, \qquad (7)$$

where $E_{\alpha\alpha'}^{\mathbf{RR}'}$ are the EBOM matrix elements from Eq. (5) and the site indices $\mathbf{R}$ and $\mathbf{R}'$ now range over the finite N sites of a sufficiently large supercell. In our present sp^3 basis, the eigenstates and eigenenergies of Eq. (7) are obtained as the solutions of a $8N \times 8N$ matrix eigenvalue problem. According to Refs. 18 and 19, a nanostructure made of one material A embedded in a barrier of material B can be modeled by using the matrix elements of the A material for the corresponding lattice sites and vice versa. For the interface, a linear interpolation of the corresponding hopping matrix elements is used. The confinement potential for the carriers can properly be incorporated by an upward shifting of the diagonal elements of the A material by the valence-band offset ΔE_v between the two materials. When the band gap between the materials B and A exceeds this offset, we are naturally left with a type-I confinement potential for the electrons and holes.

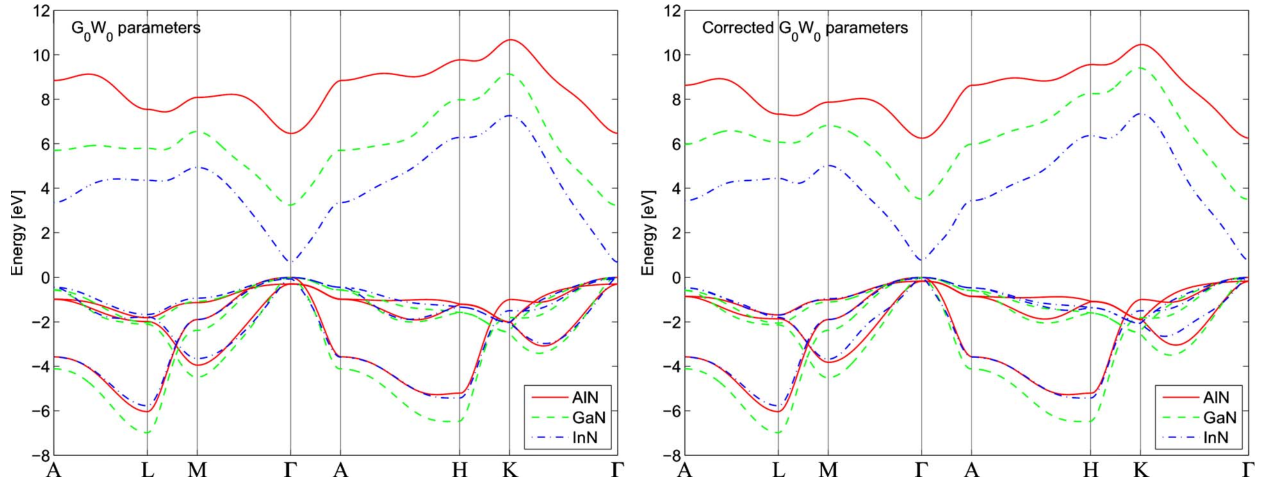

FIG. 1. (Color online) EBOM band structures for AlN, GaN, and InN with coupling up to second-nearest neighbors, using the G_0W_0 parameters (left image) and the corrected G_0W_0 parameters (right image). Further details are given in Table II and in the text. The top of the valence band is set to zero, respectively.

The application to one- or two-dimensional structures is a trivial task and can be done correspondingly.

C. Possible inclusion of piezoelectricity and strain

In the systems under consideration, there is always a spontaneous polarization due to the deviation of the c/a ratio from the value in the ideal wurtzite structure. Additionally, strain fields will influence the electronic properties of these systems, if present. While there are in fact zero-dimensional systems, such as fully relaxed nanocrystals, where this effect can be neglected, the below presented model system of epitaxially grown InN quantum dots embedded in a GaN matrix will in fact be strained due to the lattice mismatch, and this strain will not only shift the band edges but also alter the equilibrium positions of the lattice sites and thus the piezoelectric charge density.

Both, the spontaneous and the strain-induced polarization can be incorporated into the tight-binding calculations by the solution of the Poisson equation.[19,20] Although it has been discussed in previous publications such as Ref. 19, that for this specific quantum-dot system, a proper inclusion of a constant band-edge shift might be sufficient, a more general approach is of course desirable.

Again, the one-to-one correspondence to the $\mathbf{k}\cdot\mathbf{p}$ model at Γ allows for a straightforward inclusion of strain effects on the bulk band structure by augmenting the $\mathbf{k}\cdot\mathbf{p}$ Hamiltonian by a strain-dependent part, as done in Refs. 32 and 33. The then obtained analytical dependence of the EBOM matrix elements $E_{\alpha\alpha'}^{\mathbf{RR}'}$ on the deformation potentials $a_{1,2}$ of the conduction band, D_{1-6} of the valence bands, and the elastic stiffness constants can then be used either to determine a distance-dependent scaling law for the $E_{\alpha\alpha'}^{\mathbf{RR}'}$ (similar to the famous Harrison d^{-2} ansatz[39]) or directly be incorporated into the nanostructure Hamiltonian. In both cases, additionally an appropriate strain field has to be calculated for the low-dimensional system under consideration, either by atomistic[9,12] or continuum mechanical[32] approaches.

As this extension of the EBOM requires a careful comparison to further experimental and theoretical results, it is a topic of its own and part of ongoing research. Therefore, it will not furtherly be addressed in the present paper. In the following section, we will neglect the influence of piezoelectricity and strain in order to focus on the direct influence of the slightly different Kane parameters $E_p^{\parallel,\perp}$ on the single-particle results.

III. RESULTS FOR QUANTUM DOTS

A. Model quantum-dot geometry

Earlier ETBM calculations of Refs. 19 and 20 for the InN/GaN material system were performed using cubic supercells and fixed boundary conditions. In this paper, we present a different and improved kind of supercell, which is depicted

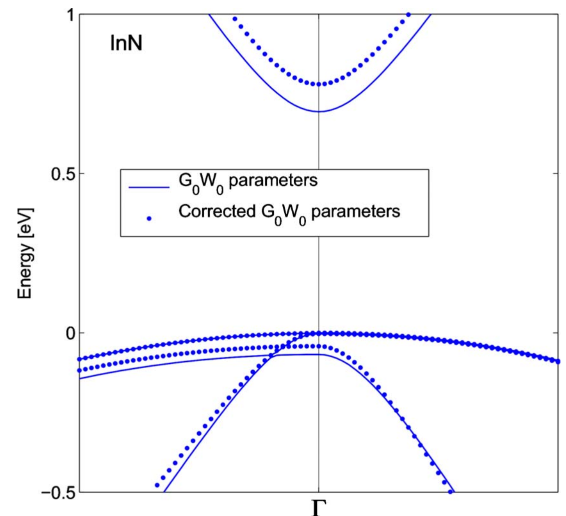

FIG. 2. (Color online) EBOM band structures for InN around Γ for the two parameter sets. Further details are again given in Table II and in caption of Fig. 1.

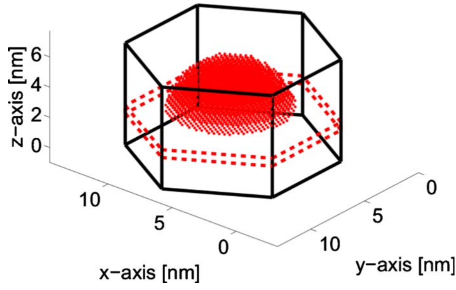

FIG. 3. (Color online) Geometry for the lens-shaped InN quantum dot on an InN wetting layer, embedded in GaN. The InN lattice sites of the QD are depicted with red dots, additionally, the intersections of the wetting layer with the boundaries of the hexagonal supercell are visualized by the dotted red lines.

in Fig. 3, by means of keeping the point-group symmetry of the underlying hexagonal Bravais lattice in combination with periodic boundary conditions. This leads to several benefits, e.g., no artificial surface states can arise in the single-particle spectrum, and in contrast to cubic supercells, our hexagonal one does not interfere with the C_{6v} point-group symmetry of the lattice. The simulated lens-shaped InN quantum dot has a diameter of 7.7 nm and a height of 3.1 nm. It is placed on top of a wetting layer with thickness of one c lattice constant since Stranski-Krastanov growth mode is assumed for the given structure. The surrounding GaN supercell has a dimension of $36.4a \times 42a \times 14c$ with respect to the Cartesian axes. With this size, convergence for the one-particle wave functions is ensured. Furthermore, a completely strained structure is supposed so that no deviations from the ideal lattice positions emerge. As valence-band offset, we use the value recommended by Vurgaftman *et al.*[37] of $\Delta E_v = 0.5$ eV for both parameter sets.

B. One-particle spectrum for embedded InN quantum dot

The numerical diagonalization of the corresponding nanostructure Hamiltonian (using the *folded spectrum method*[40]) gives the desired single-particle states and eigenenergies around the energy gap of the quantum dot. We solve Eq. (7) for eight bound electron and hole states, using the EBOM parametrization for second-nearest neighbors and taking spin-orbit coupling and crystal-field splitting into account.

The resulting eigenfunctions are visualized in Fig. 4 by isosurfaces of the probability density, supplemented by the respective eigenenergies. All states are invariant under rotations by $\frac{\pi}{3}$ around the growth direction, according to the C_{6v} point-group symmetry of the Bravais lattice. Each state is once again twofold degenerate due to time-reversal symmetry and well localized within the InN quantum dot. Table III reveals that the electron states mainly stem from the s-like conduction band so a classification by their nodal structure is possible. ψ_1^e is s-like while ψ_2^e and ψ_3^e are complex linear combinations of the form $p_{\pm} = \frac{1}{\sqrt{2}}(p_x \pm i p_y)$. ψ_4^e is a p_z-like state but distorted by the shape of the quantum dot. The hole states show similar transformation properties at first glance. Nevertheless, Table III reveals that at least two atomic p states contribute to their formation so that they underlie

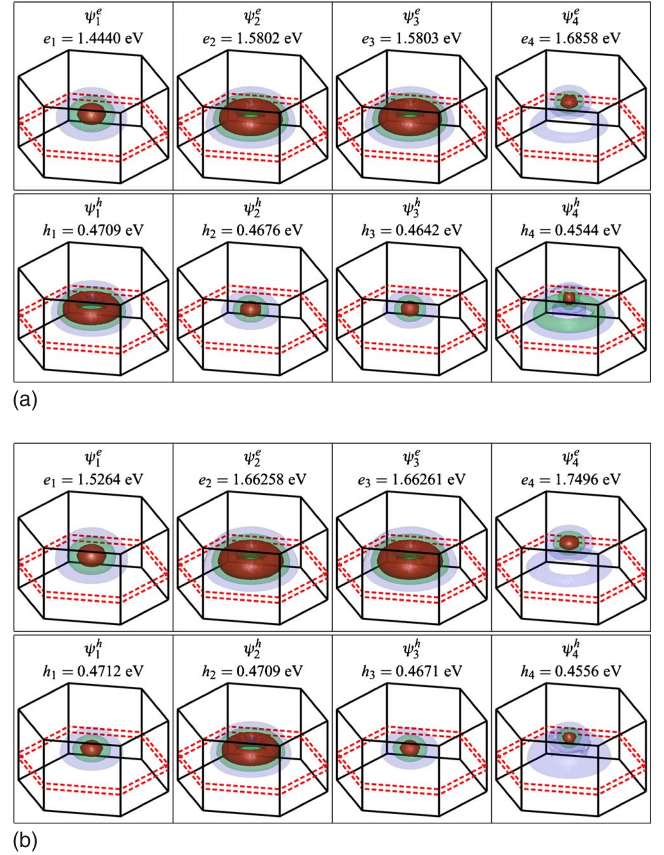

FIG. 4. (Color online) Visualization of the probability density by isosurfaces of 75% (red), 45% (green), and 15% (blue) of the maximum value for electron ψ_i^e and hole ψ_i^h states within the hexagonal supercell. The red dotted lines give the intersection of the wetting layer with the cell boundary. In addition, the corresponding one-particle eigenenergies are shown. All energies are given with respect to the valence band edge of GaN. The two parameter sets have been presented in Table II. Please note the interchanging of the states h_1 and h_2 when using the latter set of parameters.

strong band-mixing effects. This is in agreement with results from several other multiband calculations.[9,41]

By taking a closer look at the degeneracies in Fig. 4, we notice no fourfold degeneracy of ψ_2^e and ψ_3^e, in contrast to $\mathbf{k} \cdot \mathbf{p}$ calculations from Ref. 32 but reproduce the findings of earlier ETBM calculations from Ref. 21, showing a twofold degeneracy for each bound state. The latter reference also includes a detailed group theoretical discussion of this issue. The only deviations we can report on are the fact that the EBOM eigenenergies of the electrons are more strongly bound for both parameter sets, compared to other ETBM results from Refs. 19 and 20. This discrepancy can safely be attributed to the once again different set of input parameters and thus does not contradict comparative studies from Refs. 42 and 43 for zinc-blende nanostructures, which show a very good agreement between these approaches. Our results for the hole energies agree well with the earlier calculations of Refs. 19 and 20 if the piezoelectric field is neglected (see, e.g., Ref. 19 for details).

A striking feature is the different order of the hole levels when switching between the parameter sets. The torus-

TABLE III. Orbital contributions of the sp^3 basis to the bound one-particle states, calculated by summation over the site and the spin index of the projections $\langle \mathbf{R},\alpha|\psi\rangle$. Dominant parts are marked in bold.

	e_1	e_2	e_3	e_4	h_1	h_2	h_3	h_4
G_0W_0 parameters								
s	**0.878**	**0.839**	**0.839**	**0.843**	0.000	0.004	0.002	0.001
p_x	0.033	0.056	0.056	0.034	**0.499**	**0.492**	**0.494**	**0.495**
p_y	0.033	0.056	0.056	0.034	**0.499**	**0.492**	**0.494**	**0.495**
p_z	0.057	0.049	0.049	0.088	0.001	0.012	0.010	0.009
Corrected G_0W_0 parameters								
s	**0.858**	**0.812**	**0.812**	**0.818**	0.005	0.000	0.004	0.001
p_x	0.036	0.063	0.063	0.032	**0.490**	**0.497**	**0.491**	**0.490**
p_y	0.036	0.063	0.063	0.032	**0.490**	**0.497**	**0.491**	**0.490**
p_z	0.070	0.063	0.063	0.118	0.014	0.003	0.015	0.019

shaped probability density belongs to the hole ground state ψ_1^h with the G_0W_0 parameters but is found as the first excited hole state ψ_2^h when using the corrected G_0W_0 parameters. Another look at Table II reveals that the band gap of the dot material differs by less than 90 meV between these parameter sets; the confinement potential for the holes is even identical in both cases, as the same valence-band offset is used. The crystal-field splitting only differs by approximately 20 meV for both materials. Obviously, this rather small variation in the bulk band gap and the crystal-field splitting, which also results in slightly different Kane parameters $E_p^{\parallel,\perp}$ (see Appendix), suffices to change the level structure. Further studies (not shown) reveal that even variations in the order of magnitude of the accuracy of the input parameters can change the order. In addition, the differing bulk band gaps of the two parameter sets lead to slightly different one-particle energy gaps $E_g^{QD}=e_1-h_1$ of $\sim$0.97 eV (G_0W_0 parameters) and $\sim$1.05 eV (corrected G_0W_0 parameters), respectively. When calculating optical properties such as the excitonic absorption spectrum from the tight-binding single-particle spectrum, as, e.g., done in Refs. 19 and 43, the level structure and E_g^{QD} are important characteristics. A change in the first will give rise to a change in the respective dipole matrix elements between the electron and hole states and thus alter the line intensity while a change in E_g^{QD} directly shifts the energetic position of the line itself.

As the variation in the dot size and the proper implementation of strain effects and electrostatic built-in fields can additionally alter the level ordering, the influence of different material parameters should be carefully investigated when discussing the optical selection rules for a given geometry. For the system under consideration, we recommend the use of the corrected G_0W_0 parameters.

IV. CONCLUSION AND OUTLOOK

In this paper, we have presented a multiband empirical tight-binding parametrization for both bulk semiconductors and nanostructures with a wurtzite structure, which represents an adaption of the EBOM for the hexagonal phase. A basis set of one s and three p orbitals for each spin direction is placed on the sites of the underlying hexagonal Bravais lattice. Coupling up to second-nearest neighbors has been used to fit one conduction and three valence bands to the energies and curvatures at the Γ point and, additionally, to the energies at high-symmetry points throughout the whole Brillouin zone. The resulting band structures of the III-V compounds InN, GaN, and AlN were shown for two distinct parameter sets, namely, the newest G_0W_0 results by Rinke *et al.* and a slightly modified set in which we adjusted single critical parameters by replacing them by the values given by Vurgaftman *et al.* in order to obtain better agreement to experimental results.

In addition, we demonstrated the application of this parametrization to low-dimensional structures. A lens-shaped InN quantum dot on an InN wetting layer, embedded in a GaN matrix, has been modeled within a hexagonally shaped supercell with periodic boundary conditions. We have compared the resulting one-particle spectrum and the corresponding eigenstates to previous tight-binding results and have found a good concordance within the framework of the respective model. Furthermore, we have found that the two parameter sets yield a different order of hole states for the given dot diameter, although the corresponding bulk band structures barely differ at first glance. We strongly approve a careful review of the set of material parameters used in such calculations. For the present InN/GaN quantum dot system, we recommend the use of the corrected G_0W_0 parameter set.

Besides the application to other quantum-dot systems, such as GaN in AlN or different geometries, such as coupled QDs or spherical nanocrystals, the present parametrization can easily be applied to one-dimensional (quantum wires) or two-dimensional (quantum wells and superlattices) structures. Moreover, the effects of strain and piezoelectric built-in fields can be incorporated on different levels of sophistication, as suggested in the second section of this paper.

ACKNOWLEDGMENTS

The authors would like to thank Patrick Rinke for the

provision of additional G_0W_0 results at further high-symmetry points of the Brillouin zone. Furthermore, we thank Stefan Schulz for fruitful discussions. This work has been supported by the Deutsche Forschungsgemeinschaft (research group Physics of nitride-based, nanostructured, light-emitting devices, project Cz 31/14-3).

APPENDIX: EBOM PARAMETRIZATION FOR THE HEXAGONAL LATTICE

The analytical dependence of the parameters

$$P_{\parallel,\perp} = \sqrt{\frac{\hbar^2}{2m_0}E_p^{\parallel,\perp}} \tag{A1}$$

of the band gap E_g, the spin-orbit, and crystal-field splittings Δ_{so}, Δ_{cr}, and the effective masses $m_e^{\parallel,\perp}$ is given by the following two equations:[33]

$$P_\parallel^2 = \frac{\hbar^2}{2m_0}\left(\frac{m_0}{m_e^\parallel} - 1\right)\frac{3E_g(\Delta_{so}+E_g)+\Delta_{cr}(2\Delta_{so}+3E_g)}{2\Delta_{so}+3E_g}, \tag{A2}$$

$$P_\perp^2 = \frac{\hbar^2}{2m_0}\left(\frac{m_0}{m_e^\perp} - 1\right)E_g\frac{[3E_g(\Delta_{so}+E_g)+\Delta_{cr}(2\Delta_{so}+3E_g)]}{\Delta_{cr}\Delta_{so}+3\Delta_{cr}E_g+2\Delta_{so}E_g+3E_g^2}. \tag{A3}$$

The EBOM parametrization scheme with coupling up to second-nearest neighbors gives a set of equations which link the parameters of Table II to the EBOM matrix elements $E_{\alpha\alpha'}^{\mathbf{RR}'}$ of Eq. (5). To obtain the desired number of free parameters for a one-to-one correspondence, one has to apply an adequate decomposition of the $E_{\alpha\alpha'}^{\mathbf{RR}'}$ into two- and three-center integrals, following the guidelines of Ref. 25. As the explicit solution is straightforward, but very unhandy in print, it shall not be given here in full form. Instead, further details will be made accessible as supplementary material to this paper in mathematical notation in Ref. 44 and, additionally, the explicit solution as MATLAB-compatible pseudocode in Ref. 45 so that it can easily be used for own computations.

In order to give at least a brief insight into the physical meaning of the $E_{\alpha\alpha'}^{\mathbf{RR}'}$, we will give the results of the expansion of Eq. (4) to second order in $\mathbf{k}$. In this limit, the EBOM and the $\mathbf{k}\cdot\mathbf{p}$ presentation become equivalent. The following set of equations gives the EBOM matrix elements in terms of the parameters that were used in the eight-band $\mathbf{k}\cdot\mathbf{p}$ Hamiltonian of Refs. 32 and 33, where the A_i are Luttinger-type parameters which are connected to the anisotropic effective valence-band masses. For the sake of simplicity, the parameter A_7 has been set to zero in our approach. Its influence has turned out to be negligible.[46] The upper index in $E_{\alpha\alpha'}^{(k,l,m)}$ now denotes $\mathbf{R}'-\mathbf{R}$ in units of half the lattice constants a or c, respectively, so that

$$\mathbf{R}'-\mathbf{R} = \frac{ka}{2}\mathbf{e_x} + \frac{la}{2}\mathbf{e_y} + \frac{mc}{2}\mathbf{e_z},$$

$$\frac{\hbar}{2m_e^\parallel} - \frac{P_\parallel^2}{E_g} = (-4E_{ss}^{(\sqrt{3},1,2)} - 2E_{ss}^{(0,2,2)} - 4E_{ss}^{(0,0,4)} - E_{ss}^{(0,0,2)})\cdot c^2,$$

$$\frac{\hbar}{2m_e^\perp} - \frac{P_\perp^2}{E_g} = \left(-E_{ss}^{(0,2,0)} - E_{ss}^{(\sqrt{3},1,2)} - 2E_{ss}^{(0,2,2)} - \frac{1}{2}E_{ss}^{(\sqrt{3},1,0)} - 4E_{ss}^{(0,4,0)} - \frac{9}{2}E_{ss}^{(\sqrt{3},3,0)} - 2E_{ss}^{(2\sqrt{3},2,0)}\right)\cdot a^2,$$

$$\frac{\hbar}{2m_e^\perp} - \frac{P_\perp^2}{E_g} = \left(-\frac{3}{2}E_{ss}^{(\sqrt{3},1,0)} - 3E_{ss}^{(\sqrt{3},1,2)} - \frac{3}{2}E_{ss}^{(\sqrt{3},3,0)} - 6E_{ss}^{(2\sqrt{3},2,0)} - 3E_{ss}^{(2\sqrt{3},0,0)}\right)\cdot a^2,$$

$$iP_\perp = (2iE_{sx}^{(\sqrt{3},1,0)} + 4iE_{sx}^{(\sqrt{3},1,2)} + 2iE_{sx}^{(2\sqrt{3},0,0)} + 4iE_{sx}^{(2\sqrt{3},2,0)} + 2iE_{sx}^{(\sqrt{3},3,0)})\cdot a\sqrt{3},$$

$$iP_\perp = (2iE_{sy}^{(\sqrt{3},1,0)} + 2iE_{sy}^{(0,2,0)} + 4iE_{sy}^{(\sqrt{3},1,2)} + 4iE_{sy}^{(0,2,2)} + 4iE_{sy}^{(2\sqrt{3},2,0)} + 6iE_{sy}^{(\sqrt{3},3,0)} + 4iE_{sy}^{(0,4,0)})\cdot a,$$

$$iP_\parallel = (2iE_{sz}^{(0,0,2)} + 8iE_{sz}^{(\sqrt{3},1,2)} + 4iE_{sz}^{(0,2,2)} + 4iE_{sz}^{(0,0,4)})\cdot c,$$

$$A_2 + A_4 + A_5 + \frac{P_\parallel^2}{E_g} = \left(-\frac{3}{2}E_{xx}^{(\sqrt{3},1,0)} - 3E_{xx}^{(\sqrt{3},1,2)} - \frac{3}{2}E_{xx}^{(\sqrt{3},3,0)} - 6E_{xx}^{(2\sqrt{3},2,0)} - 3E_{xx}^{(2\sqrt{3},0,0)}\right)\cdot a^2,$$

$$A_2 + A_4 - A_5 = \left(-E_{xx}^{(0,2,0)} - E_{xx}^{(\sqrt{3},1,2)} - 2E_{xx}^{(0,2,2)} - \frac{1}{2}E_{xx}^{(\sqrt{3},1,0)} - 4E_{xx}^{(0,4,0)} - \frac{9}{2}E_{xx}^{(\sqrt{3},3,0)} - 2E_{xx}^{(2\sqrt{3},2,0)}\right)\cdot a^2,$$

$$A_1 + A_3 = (-4E_{xx}^{(\sqrt{3},1,2)} - 2E_{xx}^{(0,2,2)} - 4E_{xx}^{(0,0,4)} - E_{xx}^{(0,0,2)})\cdot c^2,$$

$$2A_5 + \frac{P_\parallel^2}{E_g} = (-E_{xy}^{(\sqrt{3},1,0)} - 2E_{xy}^{(\sqrt{3},1,2)} - 4E_{xy}^{(2\sqrt{3},2,0)} - 3E_{xy}^{(\sqrt{3},3,0)})\cdot a^2\sqrt{3},$$

$$\sqrt{2}A_6 + \frac{P_\parallel P_\perp}{E_g} = -4E_{xz}^{(\sqrt{3},1,2)}\cdot a\sqrt{3}c,$$

$$A_2 + A_4 - A_5 = \left(-\frac{3}{2}E_{yy}^{(\sqrt{3},1,0)} - 3E_{yy}^{(\sqrt{3},1,2)} - \frac{3}{2}E_{yy}^{(\sqrt{3},3,0)} - 6E_{yy}^{(2\sqrt{3},2,0)} - 3E_{yy}^{(2\sqrt{3},0,0)}\right)\cdot a^2,$$

$$A_2 + A_4 + A_5 + \frac{P_\parallel^2}{E_g} = \Big(- E_{yy}^{(0,2,0)} - E_{yy}^{(\sqrt{3},1,2)} - 2E_{yy}^{(0,2,2)} - \frac{1}{2}E_{yy}^{(\sqrt{3},1,0)} - 4E_{yy}^{(0,4,0)} - \frac{9}{2}E_{yy}^{(\sqrt{3},3,0)} - 2E_{yy}^{(2\sqrt{3},2,0)} \Big) \cdot a^2,$$

$$A_1 + A_3 = (- 4E_{yy}^{(\sqrt{3},1,2)} - 2E_{yy}^{(0,2,2)} - 4E_{yy}^{(0,0,4)} - E_{yy}^{(0,0,2)}) \cdot c^2,$$

$$\sqrt{2}A_6 + \frac{P_\parallel P_\perp}{E_g} = (- 4E_{yz}^{(\sqrt{3},1,2)} - 4E_{yz}^{(0,2,2)}) \cdot ac,$$

$$A_2 = \Big(- \frac{3}{2}E_{zz}^{(\sqrt{3},1,0)} - 3E_{zz}^{(\sqrt{3},1,2)} - \frac{3}{2}E_{zz}^{(\sqrt{3},3,0)} - 6E_{zz}^{(2\sqrt{3},2,0)} - 3E_{zz}^{(2\sqrt{3},0,0)} \Big) \cdot a^2,$$

$$A_2 = \Big(- E_{zz}^{(0,2,0)} - E_{zz}^{(\sqrt{3},1,2)} - 2E_{zz}^{(0,2,2)} - \frac{1}{2}E_{zz}^{(\sqrt{3},1,0)} - 4E_{zz}^{(0,4,0)} - \frac{9}{2}E_{zz}^{(\sqrt{3},3,0)} - 2E_{zz}^{(2\sqrt{3},2,0)} \Big) \cdot a^2,$$

$$A_1 + \frac{P_\perp^2}{E_g} = (- 4E_{zz}^{(\sqrt{3},1,2)} - 2E_{zz}^{(0,2,2)} - 4E_{zz}^{(0,0,4)} - E_{zz}^{(0,0,2)}) \cdot c^2. \quad \text{(A4)}$$

*dmourad@itp.uni-bremen.de

[1] A. A. Guzelian, U. Banin, A. V. Kadavanich, X. Peng, and A. P. Alivisatos, Appl. Phys. Lett. **69**, 1432 (1996).
[2] P. Michler, *Single Semiconductor Quantum Dots*, 1st ed. (Springer, New York, 2009).
[3] M. Bruchez, Jr., M. Moronne, P. Gin, S. Weiss, and A. P. Alivisatos, Science **281**, 2013 (1998).
[4] X. Michalet, F. F. Pinaud, L. A. Bentolila, J. M. Tsay, S. Doose, J. J. Li, G. Sundaresan, A. M. Wu, S. S. Gambhir, and S. Weiss, Science **307**, 538 (2005).
[5] S. Lazar, C. Hébert, and H. W. Zandbergen, Ultramicroscopy **98**, 249 (2004).
[6] M. Grundmann, O. Stier, and D. Bimberg, Phys. Rev. B **52**, 11969 (1995).
[7] A. Wojs, P. Hawrylak, S. Fafard, and L. Jacak, Phys. Rev. B **54**, 5604 (1996).
[8] J. Shi and Z. Gan, J. Appl. Phys. **94**, 407 (2003).
[9] V. A. Fonoberov and A. A. Balandin, J. Appl. Phys. **94**, 7178 (2003).
[10] C. Pryor, Phys. Rev. B **57**, 7190 (1998).
[11] O. Stier, M. Grundmann, and D. Bimberg, Phys. Rev. B **59**, 5688 (1999).
[12] A. D. Andreev and E. P. O'Reilly, Phys. Rev. B **62**, 15851 (2000).
[13] L. W. Wang and A. Zunger, Phys. Rev. B **53**, 9579 (1996).
[14] L. W. Wang and A. Zunger, Phys. Rev. B **59**, 15806 (1999).
[15] L. W. Wang, A. J. Williamson, A. Zunger, H. Jiang, and J. Singh, Appl. Phys. Lett. **76**, 339 (2000).
[16] G. Bester and A. Zunger, Phys. Rev. B **71**, 045318 (2005).
[17] R. Santoprete, B. Koiller, R. B. Capaz, P. Kratzer, Q. K. K. Liu, and M. Scheffler, Phys. Rev. B **68**, 235311 (2003).
[18] S. Schulz and G. Czycholl, Phys. Rev. B **72**, 165317 (2005).
[19] S. Schulz, S. Schumacher, and G. Czycholl, Phys. Rev. B **73**, 245327 (2006).
[20] S. Schulz and G. Czycholl, Phys. Status Solidi C **3**, 1675 (2006).
[21] S. Schulz, S. Schumacher, and G. Czycholl, Eur. Phys. J. B **64**, 51 (2008).
[22] M. Korkusinski, P. Hawrylak, M. Zielinski, W. Sheng, and G. Klimeck, Microelectron. J. **39**, 318 (2008).
[23] P. Rinke, M. Scheffler, A. Qteish, M. Winkelnkemper, D. Bimberg, and J. Neugebauer, Appl. Phys. Lett. **89**, 161919 (2006).
[24] P. Rinke, M. Winkelnkemper, A. Qteish, D. Bimberg, J. Neugebauer, and M. Scheffler, Phys. Rev. B **77**, 075202 (2008).
[25] J. C. Slater and G. F. Koster, Phys. Rev. **94**, 1498 (1954).
[26] Y. C. Chang, Phys. Rev. B **37**, 8215 (1988).
[27] J. P. Loehr, Phys. Rev. B **50**, 5429 (1994).
[28] D. Fritsch, H. Schmidt, and M. Grundmann, Phys. Rev. B **69**, 165204 (2004).
[29] C. Chen, Phys. Lett. A **329**, 136 (2004).
[30] X. Cartoixà, D. Z.-Y. Ting, and T. C. McGill, Phys. Rev. B **68**, 235319 (2003).
[31] D. J. Chadi, Phys. Rev. B **16**, 790 (1977).
[32] M. Winkelnkemper, A. Schliwa, and D. Bimberg, Phys. Rev. B **74**, 155322 (2006).
[33] S. L. Chuang and C. S. Chang, Phys. Rev. B **54**, 2491 (1996).
[34] Y. C. Yeo, T. C. Chong, and M. F. Li, J. Appl. Phys. **83**, 1429 (1998).
[35] P. Rinke, A. Qteish, J. Neugebauer, C. Freysoldt, and M. Scheffler, New J. Phys. **7**, 126 (2005).
[36] P. Rinke (private communication).
[37] I. Vurgaftman and J. R. Meyer, J. Appl. Phys. **94**, 3675 (2003).
[38] M. Winkelnkemper, R. Seguin, S. Rodt, A. Schliwa, L. Reissmann, A. Strittmatter, A. Hoffmann, and D. Bimberg, J. Appl. Phys. **101**, 113708 (2007).
[39] S. Froyen and W. A. Harrison, Phys. Rev. B **20**, 2420 (1979).
[40] L. Wang and A. Zunger, J. Chem. Phys. **100**, 2394 (1994).
[41] S. Wei and A. Zunger, Appl. Phys. Lett. **69**, 2719 (1996).
[42] O. Marquardt, D. Mourad, S. Schulz, T. Hickel, G. Czycholl, and J. Neugebauer, Phys. Rev. B **78**, 235302 (2008).
[43] S. Schulz, D. Mourad, and G. Czycholl, Phys. Rev. B **80**, 165405 (2009).
[44] See supplementary material at http://link.aps.org/supplemental/10.1103/PhysRevB.81.165316 for further details of the parametrization.
[45] See supplementary material at http://link.aps.org/supplemental/10.1103/PhysRevB.81.165316 for the explicit solution of the resulting system of equations.
[46] D. J. Dugdale, S. Brand, and R. A. Abram, Phys. Rev. B **61**, 12933 (2000).